Leukocyte integrin $\alpha_L\beta_2$ headpiece structures: The αI domain, the pocket for the internal ligand, and concerted movements of its loops

Mehmet Sen[a,b] and Timothy A. Springer[a,1]

[a]Program in Cellular and Molecular Medicine, Children's Hospital Boston, and Departments of Biological Chemistry and Molecular Pharmacology and of Medicine, Harvard Medical School, Boston, MA 02115; and [b]Department of Biology and Biochemistry, University of Houston, Houston, TX 77204

Contributed by Timothy A. Springer, January 29, 2016 (sent for review January 15, 2016; reviewed by Martin J. Humphries and Kai W. Wucherpfennig)

High-resolution crystal structures of the headpiece of lymphocyte function-associated antigen-1 (integrin $\alpha_L\beta_2$) reveal how the αI domain interacts with its platform formed by the α-subunit β-propeller and β-subunit βI domains. The $\alpha_L\beta_2$ structures compared with $\alpha_X\beta_2$ structures show that the αI domain, tethered through its *N*-linker and a disulfide to a stable β-ribbon pillar near the center of the platform, can undergo remarkable pivoting and tilting motions that appear buffered by *N*-glycan decorations that differ between α_L and α_X subunits. Rerefined β_2 integrin structures reveal details including pyroglutamic acid at the β_2 N terminus and bending within the EGF1 domain. Allostery is relayed to the αI domain by an internal ligand that binds to a pocket at the interface between the β-propeller and βI domains. Marked differences between the α_L and α_X subunit β-propeller domains concentrate near the binding pocket and αI domain interfaces. Remarkably, movement in allostery in the βI domain of specificity determining loop 1 (SDL1) causes concerted movement of SDL2 and thereby tightens the binding pocket for the internal ligand.

Integrins are α/β heterodimeric metallo-receptors that bidirectionally transduce chemical cues together with mechanical forces across cell membranes (1). The β_2 integrin subfamily contains lymphocyte function-associated antigen-1 (LFA-1, integrin $\alpha_L\beta_2$), complement receptor 3 (CR3, $\alpha_M\beta_2$, Mac-1), CR4 ($\alpha_X\beta_2$, p150,95), and $\alpha_D\beta_2$ and is exclusively expressed on leukocyte lineages (2). LFA-1 on the surface of lymphocytes, natural killer cells, neutrophils, and monocytes binds to intercellular adhesion molecules (ICAMs) on the surface of other cells to mediate adaptive and innate immune responses, trafficking across endothelium, and migration within tissues (3). Leukocyte adhesion deficiency (4) and clinical approval of an antibody to LFA-1 to treat autoimmunity (5) illustrate the immunological significance of LFA-1 interaction with ICAMs.

β_2 integrin α subunits contain an inserted (αI) domain that binds to external ligands such as ICAMs. Crystal and NMR structures have revealed open/high-affinity and closed/low-affinity conformations of the LFA-1 αI domain, how it binds to ICAMs, and its dynamics, but only in isolation from other integrin domains (6–12). Here, we characterize crystal structures of the LFA-1 headpiece and rerefine previous $\alpha_X\beta_2$ ectodomain (13) and β_2 leg fragment (14, 15) crystal structures. The LFA-1 αI domain adopts a markedly different orientation relative to the remainder of the integrin head than seen with $\alpha_X\beta_2$ (13, 16) and suggests that a surprising range of αI domain orientations are compatible with relay of allostery. We also find that the βI domain SDL2 loop in β_2 integrins moves in allostery and describe the responsible SDL1–SDL2 interactions, which are present in only a subset of integrin β subunits.

Results and Discussion

Structures of the LFA-1 Headpiece. We crystallized an LFA-1 headpiece containing the α_L-subunit αI and β-propeller domains and β_2-subunit βI, hybrid, PSI, and EGF1 domains in PEG with either Mg formate (pH 6.8), Tris (pH 8), or Mes (pH 6.5). Diffraction extended to limits of 2.5, 2.15, and 2.9 Å, respectively, and structures were refined to R_{free} of 0.225–0.234 (Fig. 1*A* and Table S1). Deletion of three *N*-linked glycosylation sites and proteolytic removal of the flexible thigh domain (13) contributed to achieving high resolution.

Whereas αI-less integrins bind ligands at a β-propeller interface with the βI domain, αI integrins bind ligands at the αI domain and bind an internal ligand at the β-propeller interface with the βI domain (1). Integrin αI and βI domains are structurally homologous and bind an acidic residue in ligands to an Mg^{2+} ion held in a metal ion-dependent adhesion site (MIDAS). Unlike the αI MIDAS, the βI MIDAS is flanked by two Ca^{2+}-binding sites, the adjacent to MIDAS (ADMIDAS) and synergistic metal ion-binding site (SyMBS) (Fig. 1*B*). Mg^{2+} and Ca^{2+} were present in the protein buffer used for crystallization but were omitted from solutions used to soak crystals for cryopreservation. Interestingly, Mg^{2+} was lost from the βI MIDAS and retained at the αI MIDAS in crystals with Tris and Mes and retained at both sites in crystals with Mg formate (Fig. 1*B*). The selective loss of Mg^{2+} from the βI MIDAS is consistent with sensitivity of the three metal ions of βI domains to crystallization conditions (17).

For comparisons here, we reprocessed to higher resolution and rerefined an $\alpha_X\beta_2$ ectodomain crystal structure with four closed, bent ectodomain molecules, one of which has density for the αI domain. Despite extending the resolution from 3.56 to 3.3Å, with help from Phenix.Rosetta (18) the R_{free} dropped from 33.5% to 30.8% (Table S2). These previous closed β_2 integrin structures lacked βI domain MIDAS and SyMBS metal ions. The 2.5 Å headpiece structure reported here with its full complement of βI domain metal ions and the highly similar 2.15 Å LFA-1 headpiece structure now enable detailed comparisons of the closed β_2 βI domain to the previously reported 2.75 Å internally liganded, cocked $\alpha_X\beta_2$ βI domain. We also rerefined high-resolution β_2 leg fragment structures that extend from the PSI domain to EGF domain 1, 2, or 3 but lack the βI domain (14, 15) (Table S2).

Significance

αI integrins have 13 extracellular domains in two subunits; communication between these domains is key to regulating affinity. Structures of integrins that contain a special ligand-binding domain, the αI domain, reveal it is linked in a highly flexible manner to the β-propeller domain. Differences among αI integrin β-propeller domains concentrate at the interface with the αI domain and the binding pocket for an internal ligand that relays allostery between αI and βI domains. We reveal in many integrins a mechanism by which allostery can be communicated by concerted motions of two loops that form the interface in the βI domain for both internal and external ligands. The motions markedly increase complementarity for ligands.

Author contributions: T.A.S. and M.S. designed research; M.S. performed research; T.A.S. and M.S. analyzed data; and T.A.S. and M.S. wrote the paper.

Reviewers: M.J.H., University of Manchester; and K.W.W., Dana-Farber Cancer Institute.

The authors declare no conflict of interest.

Data deposition: The crystallography, atomic coordinates, and structure factors have been deposited in the Protein Data Bank, www.pdb.org (PDB ID codes 5E6R, 5E6S, 5E6U–5E6X, and 5ES4).

[1]To whom correspondence should be addressed. Email: Timothy.Springer@childrens.harvard.edu.

This article contains supporting information online at www.pnas.org/lookup/suppl/doi:10.1073/pnas.1601379113/-/DCSupplemental.

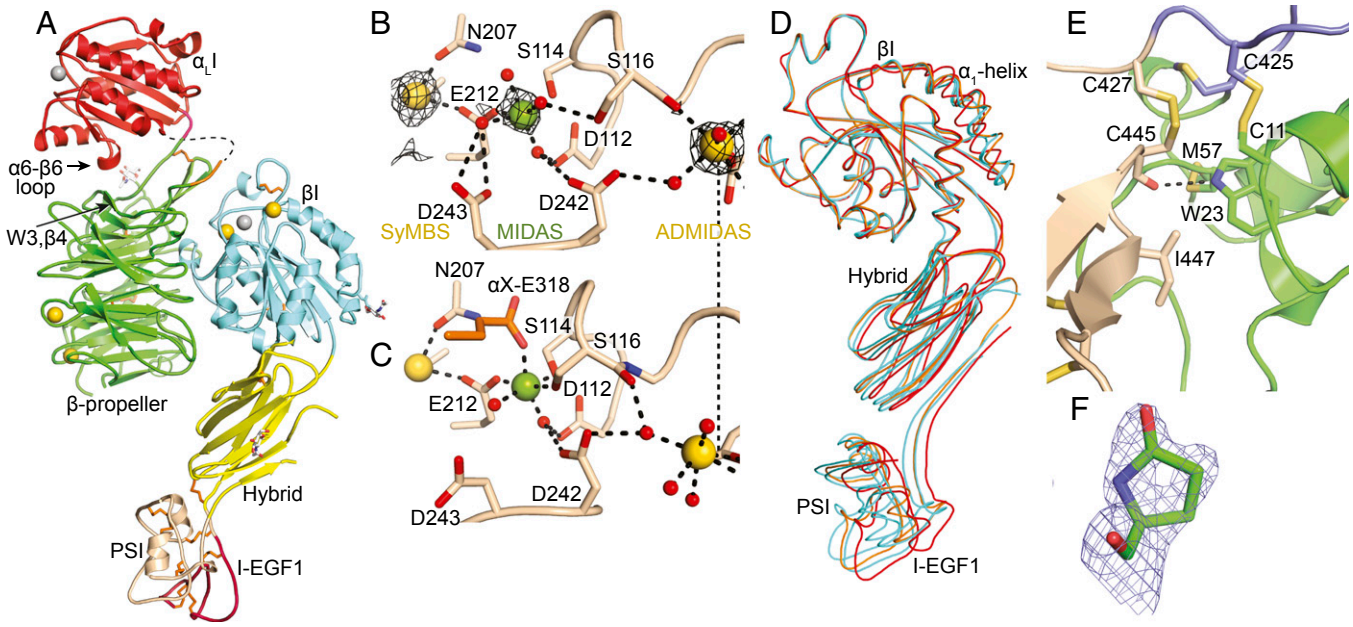

Fig. 1. LFA-1 headpiece structure. (*A*) Representative LFA-1 headpiece structure [crystal in Mg formate, Protein Data Bank (PDB) ID code 5E6U]. Ribbon cartoon with disulfides as gold sticks, glycans as white sticks with red oxygens, and Ca^{2+} and Mg^{2+} as gold and silver spheres, respectively. βI domain metal binding sites of (*B*) LFA-1 crystal in Mg formate and (*C*) internally liganded $\alpha_X\beta_2$ crystal (PDB ID code 4NEH). (*D*) β-subunit domain orientation differences shown after superposition on the βI domain of the two most dissimilar LFA-1 headpiece examples (cyan, PDB ID codes 5E6S and 5E6U), rerefined closed–bent $\alpha_X\beta_2$ ectodomain (orange, PDB ID code 5ES4), and internally liganded bent $\alpha_X\beta_2$ ectodomain (red). (*E*) Interface between the PSI (green) and I-EGF1 (wheat) domains in PDB ID code 5E6U. (*F*) N-terminal pyroglutamic acid (PDB ID code 5E6V). Mesh shows 1σ 2Fo–Fc density.

The LFA-1 headpiece structures have closed conformations. The αI domain MIDAS Mg^{2+}coordination (Fig. S1*A*) and positions of the αI domain β1–α1 loop, α1-helix, β6–α7 loop, and α7-helix all evidence the closed state (8). The β-subunit hybrid domain is swung in toward the α subunit in the closed conformation (Fig. 1*A*). The closed βI domain shows strong densities for Ca^{2+} at the SyMBS and ADMIDAS, Mg^{2+} in the MIDAS, and metal coordinating waters (Fig. 1*B*). Moreover, an auxiliary MIDAS residue, Asp-243, coordinates the MIDAS Mg^{2+} through an intermediate water (Fig. 1*B*). This side chain orients away from the MIDAS in internally liganded $\alpha_X\beta_2$ (Fig. 1*C*). The LFA-1 βI domain β1–α1 loop, α1-helix, β6–α7 loop, and α7-helix have conformations essentially identical to those in closed β1, β3, β6, and β7 integrin structures (19–23).

Apart from variation in bound metal ions, the five examples of the LFA-1 headpiece seen here in three crystal asymmetric units have almost identical lattice contacts (Fig. S1*D*) and similar structures, except for differences in orientation between the βI, hybrid, PSI, and EGF1 domains (Fig. 1*D*). Similar overall orientation, and variation in interdomain orientation, is seen among examples of $\alpha_x\beta_2$ ectodomains (Fig. 1*D*). In the upper β-leg, the PSI and EGF1 domains link to the C and *N* termini of the hybrid domain at its same end, opposite the βI domain (Fig. 1*A*). Remarkably, the PSI and EGF1 domains each vary by >20° in orientation with respect to the hybrid domain among structures yet vary little in orientation relative to one another. The motions of the β_2 PSI and EGF1 domains are correlated with one another through a hydrophobic interface that includes the PSI domain Cys11–Cys425 disulfide, the EGF1 domain Cys427–Cys445 disulfide, EGF1 residue Ile447, and PSI residues Met57 and Trp23 (Fig. 1*E*). Trp23 additionally has a side-chain hydrogen bond to the EGF1 Cys445 backbone. The interface described here provides a mechanism for preserving the relative orientation between the PSI domain and the N-terminal end of EGF1 in all β_2 integrin crystal structures described to date, including the three rerefined β_2 leg fragments. However, EGF1 lacks one disulfide (C2–C4) relative to the integrin EGF 2, 3, and 4 domains. Interestingly, this allows the C-terminal end of EGF1 to flex remarkably relative to its N-terminal end in one β_2 leg fragment structure (Fig. S1*C*). The C1–C5 disulfide at the N-terminal end and the C3–C6 and C7–C8 disulfides at the C-terminal end of EGF1 retain typical orientations within the domain (20). Flexion occurs in between, where the C2–C4 disulfide locates in other integrin EGF domains, and may be facilitated by the absence of this disulfide. Flexion in EGF1 is distinct from the previously described flexion within the C1–C5 disulfide at the tip of EGF2, where C5 keeps its position and the position of C1 changes greatly (20).

Protein sequencing of the integrin β_2 subunit showed that its N terminus is blocked (24). Unusually good electron density at the N terminus of the PSI domain allowed us to build pyroglutamic acid at position 1 in one rerefined β_2-leg structure (Fig. 1*F*). The N-terminal glutamine is thus blocked by cyclization of its side chain with its α-amino group.

αI Domain Flexibility. The β-propeller and βI domains form a platform, above which the αI domain can rotate and tilt. The LFA-1 αI domain tilts so far toward the β-propeller that its α6–β6 loop contacts the β4 strand of β-propeller sheet W3 (Fig. 1*A*). This orientation in $\alpha_L\beta_2$ differs greatly from orientations seen previously in $\alpha_X\beta_2$ ectodomain crystal structures (Fig. 2 *A* and *B*) and together with them demonstrates remarkable αI domain flexibility. Whereas in the $\alpha_L\beta_2$ headpiece structure the αI MIDAS tilts away from the βI domain (marked by its βI MIDAS in Fig. 2*C*), the αI domain in closed, bent $\alpha_X\beta_2$ crystals tilts 150° in the opposite direction, toward the βI domain (Fig. 2*E*). Crystal lattice contacts also constrain α_L and α_X αI domain orientations, but the almost opposite orientations of the closed α_L and α_X αI domains suggest that flexibility of αI domains in vivo may only be limited by contacts with the platform.

N-glycosylation sites are prominent in the interface between the platform and the αI domain, and the attached oligosaccharides may cushion the αI domain and dampen its motion, as well as introduce some integrin-specific differences (Fig. 2 *C–E*). For example, tilting of the α_L αI domain brings it into contact with the W3 β3–β4 loop (Fig. 2*C*), which in α_X is shielded by the *N*-glycan attached to Asn373 (Fig. 2 *D* and *E*). The αI domain in $\alpha_X\beta_2$ is surrounded by four *N*-glycosylation sites at Asn-42, Asn-72, Asn-366, and Asn373 (Fig. 2 *D* and *E*). In contrast, only two β-propeller *N*-glycosylation sites at Asn-40 and Asn-64 are near the αI domain

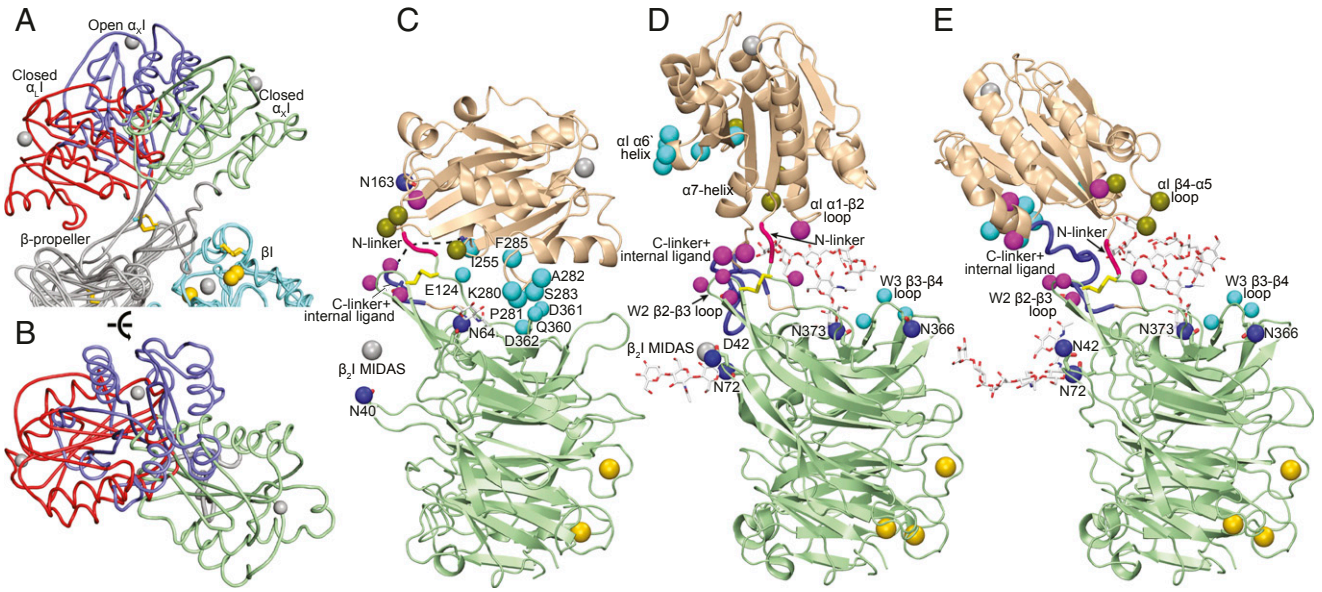

Fig. 2. αI domain orientations range widely. *A* and *B* compare αI domain position in LFA-1 headpiece (red) and $\alpha_X\beta_2$ ectodomain structures with closed (green) and open (blue) αI domains (13, 16) (PDB ID codes 5E6U, 5ES4, and 4NEH, respectively) after superimposition on the β-propeller (gray) and βI domain (cyan) in the head. *C–E* show contacts that limit αI domain orientation in the same structures with αI domain in wheat and β-propeller in light green cartoon; the βI domain is indicated schematically by the position of its MIDAS Mg^{2+} ion shown as a silver sphere. αI domain/β-propeller contacting residues are indicated with larger (αI) or smaller (β-propeller) Cβ atom spheres colored according to whether contacts are in LFA-1 with closed αI domain (cyan, *C*), $\alpha_X\beta_2$ with closed αI domain (violet, *D*), or $\alpha_X\beta_2$ with open αI domain (split pea, *E*). Homologous residues are shown in the same color in other panels. *N*-glycosylation sites are shown with Asn side chains and carbohydrate residues in stick and with Asn Nγ atoms shown as blue spheres (one Asn mutated to Asp is also shown).

in $\alpha_L\beta_2$ (Fig. 2*C*). However, the α_L αI domain has an *N*-glycosylation site at Asn-163, whereas the α_X αI domain has no *N*-linked sites. Asn-163 is in the α_L αI domain α1–β2 loop, on the platform-proximal face of the αI domain (Fig. 2*C*), and thus, an *N*-linked glycan attached here could buffer αI domain interactions with the platform.

Flexibility of the αI domain occurs in its *N*-linker and C-linker that join its N and C termini to the β-propeller. These linkers insert the αI domain between β-sheets W2 and W3 in the β-propeller. The *N*-linker is disulfide-linked to the end of the β2 strand in β-propeller blade W2 (Figs. 2 *C–E* and 3). The W2 β2 and β3 strands jut out from the β-propeller and are structurally conserved in $\alpha_L\beta_2$ and $\alpha_X\beta_2$, despite large variation in position of the disulfide-linked αI domain (Fig. 3). Thus, the W2 β2 and β3 strands form a pillar on the platform to which the *N*-linker of the αI domain is tethered. Despite being highly conserved in their cores, the α_L and α_X β-propeller domains are only 43% identical in sequence. Structural differences between the β-propeller domains concentrate in the loops of propeller blades W1, W2, and W3 that are adjacent to the αI domain insertion position between blades W2 and W3 (Fig. 3). Especially large differences in conformation between α_L and α_X are seen in the W1 β2–β3 and β4–β1 loops, the W2 β3–β4 loop, the loop joining W2 β4 to the *N*-linker, and the W3 β3–β4 loop. The W2 β2–β3 loop with its disulfide tether to the αI domain is in the midst of all these differences and thus is all the more remarkable for its structural conservation (Fig. 3).

The internal ligand and C-linker lie at the C terminus of the αI domain. In the closed αI conformation, the internal ligand comprises the five C-terminal α7-helix residues and the three following residues. In the open αI conformation, these residues completely reshape to form the internal ligand that binds a pocket at the interface of the β-propeller and βI domains (16). The following seven residues, the C-linker, link the internal ligand sequence to β-propeller blade W3. In an $\alpha_X\beta_2$ structure with the internal ligand bound to its pocket, the open αI domain adopts an orientation intermediate between the closed αI domain orientations in $\alpha_L\beta_2$ and $\alpha_X\beta_2$ structures (Fig. 2*D*). The open αI domain has few contacts with the platform except in the immediate vicinity of the linkers, and its position is stabilized by crystal lattice contacts that are specific for the open αI conformation. Two different crystal forms show that even in the internally liganded, open αI conformation, the αI domain can flex (16).

In the $\alpha_L\beta_2$ headpiece structure with its closed αI domain, the C-terminal portion of the α7-helix has substantially higher B factors than its N-terminal portion, and much of the C-linker is disordered (Fig. 4*A*). The position of the α7-helix in previous isolated α_L αI domain structures is dependent on crystal lattice contacts and differs from that in $\alpha_L\beta_2$ headpiece crystals (Fig. 4*B*), where the only lattice contact is with the side chain in the second residue of the α7-helix (Fig. S1*D*). In contrast, α7-helix positions in the headpiece crystal structure and in an NMR structure of the isolated αI domain are similar (Fig. 4*B*). The higher B factors of the C-terminal portion of the α7-helix seen here correlate well with reduced numbers of NMR distance restraints and higher rmsd among NMR ensembles (11) (Fig. 4*B*). Furthermore, residual dipole coupling and NMR relaxation experiments show that the C-terminal portion of the α7-helix has an enhanced dynamic propensity in NMR time scales and samples distinct conformations in the low affinity state (12). Moreover, in all three $\alpha_L\beta_2$ molecules in the crystal structure that extends to 2.15 Å resolution, residues ^{309}IEGT^{312} in the internal ligand (invariant in integrin $\alpha_X\beta_2$; Fig. S2*D*) and ^{313}DKQDLT^{318} in the C-linker are disordered. In the internal ligand-bound conformation of $\alpha_X\beta_2$, Glu-310 binds to the βI MIDAS, Gly-311 helps form a tight turn at Glu-310, and the side chain of Thr-312 hydrogen bonds to the backbone and stabilizes the turn. Together, the high B factors of αI domain residues 297–308 in the α7-helix including 305–308 in the internal ligand and disorder of internal ligand and C-linker residues 309–318 show that this region is dynamic. Notably, rapid dynamics in this region would facilitate sampling of conformations of the internal ligand similar to those required for binding to its pocket and thus relay of allostery.

Our study highlights distinct aspects of αI domain flexibility. First, the αI domain is tethered through its *N*-linker by a disulfide to a stout pillar, the β-propeller W2 β2–β3 ribbon, near the center of the β-propeller βI domain platform. The disulfide, *N*-linker, and

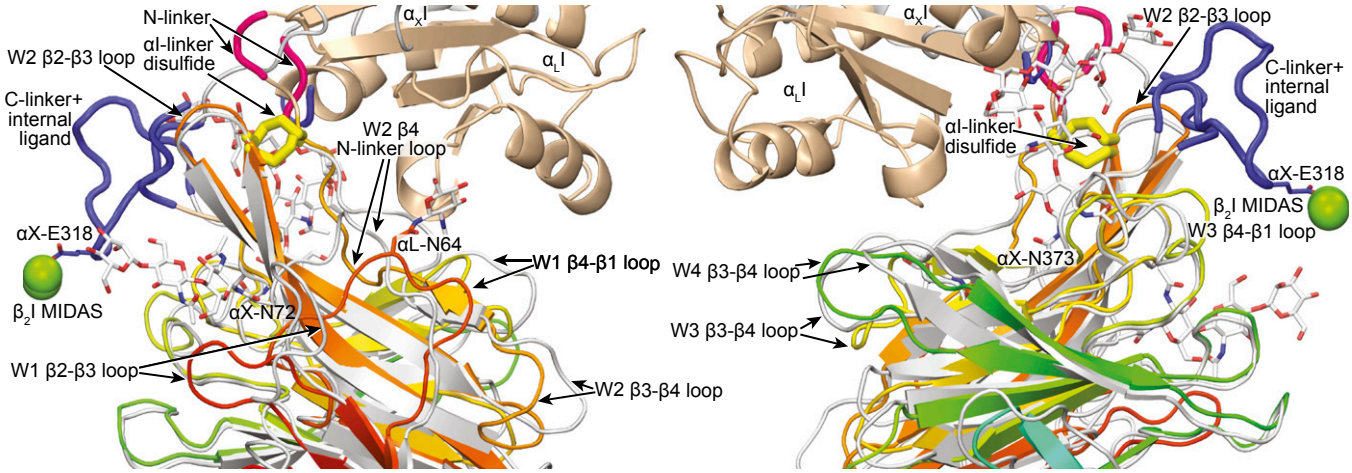

Fig. 3. Differences between the αI-proximal regions of the α_L and α_X β-propeller domains. The β-propellers are superimposed. α_L (PDB ID code 5E6U) is rainbow (β-propeller) and wheat (αI), and α_X (PDB ID code 4NEH) is gray (both domains). *N*-linkers are red, and C-linkers and internal ligand are blue. *N*-glycans are shown in stick, and the *N*-linker disulfide is shown in large yellow stick. βI MIDAS Mg^{2+} ions are shown as green spheres to indicate βI domain position.

C-linker allow marked tilting and rotation relative to the platform that appears limited only by αI domain collision with the platform. *N*-glycans decorate the platform and platform-proximal face of the αI domain and create differences among integrin α subunits but nonetheless are themselves flexible and likely do more to soften than limit αI motion. αI domain flexibility and small size compared with the platform, which binds ligands in αI-less integrins, specialize the αI domain for faster ligand binding and binding to less accessible ligands. Second, the C-terminal two-thirds of the αI domain α7-helix is more flexible than its N-terminal third. Finally, the βI MIDAS-binding portion of the internal ligand and the C-linker are disordered, even in 2.15-Å resolution crystal structures. These features may enable rapid sampling of alternative conformations, binding to the βI domain MIDAS, and transition between open and closed αI integrin conformations. According to the traction force model of integrin activation (1), this would allow activation of LFA-1 when the αI domain binds the ligand at the same time as the β-subunit cytoplasmic domain is pulled by the actin cytoskeleton, enabling the resulting tensile force exerted through the integrin to stabilize the more extended active conformation and "activate" the integrin.

α-Subunit Specificity of the Internal Ligand Pocket. The internal ligand reshapes from the integrin α subunit, and it binds to a pocket created in part by the α subunit (Fig. 5*A*). Because the local concentration of the internal ligand is high near its cognate pocket, it is highly unlikely that this pocket would bind to an internal ligand from another integrin molecule. Nonetheless, there may be α-subunit sequence specificity. Replacement of the α_L C-linker sequence SKQDLT with the α_X C-linker sequence E^{321}TTSSS decreased $\alpha_L\beta_2$ ligand binding, with most of the difference traced to α_X Glu321 (25). Moreover, β_2 integrin small-molecule antagonists that bind to the same pocket as the internal ligand can show α-subunit selectivity (26).

The $\alpha_L\beta_2$ structure indeed shows marked α-subunit differences in the internal ligand-binding pocket. The long W3 β4–β1 loop, which forms a prominence over the binding pocket, differs markedly in backbone conformation and almost completely in sequence between α_X and α_L, including at its β2-proximal tip where α_L Ala-376 replaces α_X Asp-383 (Fig. 5*A*). The *N*-glycan at Asn-373 in α_X attaches to the beginning of this loop and forms an inner lining of the pocket absent in α_L. The neighboring W3 β2–β3 loop also projects into the binding pocket with α_L Lys-346 and Asp-347 replacing α_X Phe-354 and Thr-355 (Fig. 5*A*). Next on the edge of the binding pocket is the loop between the C-linker and W3 β1. It contains highly conserved binding pocket residue α_L Phe-320/α_X Phe-328 but also residue Asn-321 in α_L that replaces Glu-329 in α_X. The large differences in shape, polarity, and charge of the internal ligand-binding pocket in α_L and α_X may explain dependence on C-linker sequence for α_L adhesive activity and the ability to obtain α-selective α/βI allosteric antagonists that bind to this pocket (25, 26). Moreover, the high-resolution structure of the internal ligand-binding pocket of $\alpha_L\beta_2$ now enables rational, structure-guided development of α-subunit–selective α/βI antagonists.

The major α-subunit differences in the binding pocket line the region where the C-linker helps bury the internal ligand and crosses over to connect to β-propeller blade W3 (Fig. 5*A*). The distinctive features described above include the *N*-glycan attached to the W3 β4–β1 loop, which is conserved in $\alpha_X\beta_2$, $\alpha_M\beta_2$, and $\alpha_D\beta_2$ and absent in $\alpha_L\beta_2$. These features may regulate both the affinity and kinetics of internal ligand binding—that is, the population of the active state and rate of sampling of the active state, respectively—in β_2 integrins.

Movement of SDL2 in Allostery. Among the three βI domain specificity-determining loops (SDLs), SDL1 contains the Asp-X-Ser-X-Ser MIDAS binding motif and ADMIDAS-coordinating residues in the β1–α1 loop and α1-helix, which move toward the ligand in transition from the closed to open βI domain conformations (27). Partial SDL1 movements toward the open conformation (intermediate

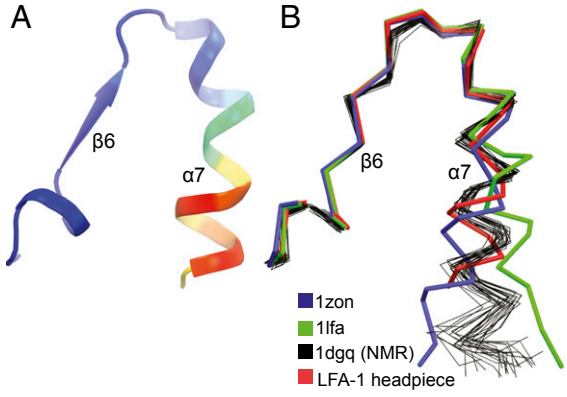

Fig. 4. αI domain α7-helix flexibility. Structures are superimposed on the αI domain with only the C-terminal portion of αI domain shown. *A* and *B* are in identical orientations. (*A*) Ribbon cartoon of the 2.15 Å $\alpha_L\beta_2$ structure colored by the Cα atom B factor from low (blue) to high (red). (*B*) Comparisons of isolated α_L αI domain crystal structures (PDB ID codes 1LFA and 1ZON) (6, 7), thick ribbon traces; isolated αI domain NMR structure (PDB ID code 1DGQ) (11), thin ensemble ribbon traces; and α_L αI domain in headpiece crystal structure, thick ribbon trace.

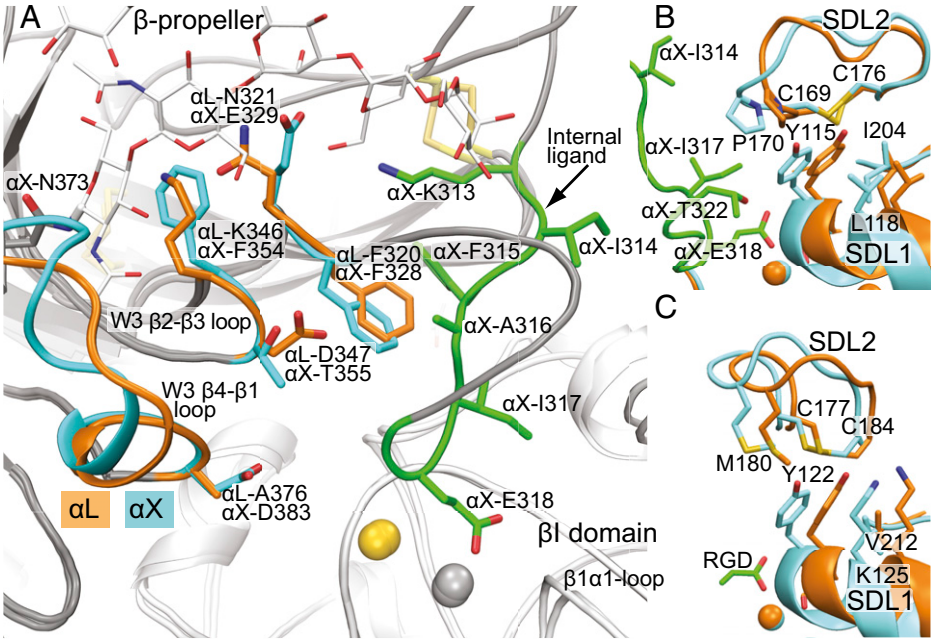

Fig. 5. The internal ligand-binding pocket and concerted movement of SDL1 and SDL2. (*A*) The internal ligand-binding pockets of the $\alpha_L\beta_2$ headpiece and internally liganded, cocked $\alpha_X\beta_2$ ectodomain after superimposition on the β-propeller and βI domains. The conserved Phe and pocket residues and backbone that differ between α_L and α_X are shown with orange (α_L) or cyan (α_X) side chains and ribbon cartoon. The internal ligand of α_X is similarly shown in green. Otherwise, α and β subunits are shown in gray and white ribbon cartoon, respectively. Metal ions are spheres in gold (SyMBS Ca^{2+}) and silver (MIDAS Mg^{2+}). (*B* and *C*) SDL1-enforced movement of SDL2 in β_2 integrins (*B*) and $\alpha_{IIb}\beta_3$ (*C*). Closed $\alpha_L\beta_2$ (PDB ID code 5E6S) and $\alpha_{IIb}\beta_3$ (PDB ID code 3T3P) conformations are in orange, whereas internally liganded, cocked $\alpha_X\beta_2$ (PDB ID code 4NEH) and open $\alpha_{IIb}\beta_3$ conformations (PDB ID code 2VDR) are in cyan (16, 30). Structures are in identical orientations and show ribbon cartoon and key side chains in stick.

conformations) are also induced when the ligand is soaked in or the internal ligand binds to integrins that are otherwise restrained in closed or bent conformations by crystal lattice contacts (16, 27).

Interestingly, comparison of our high-resolution $\alpha_L\beta_2$ headpiece structures to the 2.75 Å internally liganded intermediate "cocked" $\alpha_X\beta_2$ structure (16) now reveals substantial movement of SDL2 in addition to SDL1 in the intermediate conformation (Fig. 5*B*). The largest movement in the SDL2 loop is at the backbone and side chain of β_2 Pro-170. The movement brings the β_2 Pro-170 side chain within van der Waals contact range and close to α_X residues Ile-317 and Ile-314 in the intrinsic ligand, respectively. Notably, α_X Ile-314 is invariant and Ile-317 is invariantly hydrophobic in all nine human αI integrin α subunits (Fig. S2*D*). These residues create a hydrophobic cover for invariant α_X Glu-318, thereby strengthening the metal coordination bond between the side chain of α_X Glu-318 and the MIDAS Mg^{2+} ion (Fig. 5*B*). The movement of β_2 Pro-170 toward the intrinsic ligand markedly narrows the binding pocket and increases its complementarity, in agreement with the mutational importance of SDL2 in LFA-1 activation (28). Thus, the closed $\alpha_L\beta_2$ structure enables insights into the process of shape-shifting toward the open, high-affinity integrin conformation.

SDL2 shape-shifting is enforced by the side chain of Tyr-115 in SDL1 (Fig. 5*B*). There are no α-subunit–specific SDL2 contacts or crystal lattice contacts that could provide alternative explanations for SDL2 movement (Fig. S1*D*). Tyr-115 locates between the two Ser residues of the MIDAS motif, Ser-114 and Ser-116, and thus its backbone is constrained to move with SDL1 in shape-shifting. Moreover, the side chain of Tyr-115 is confined to a single rotamer by close interaction with surrounding residues, including βI domain residues Leu-118 in the α1-helix, Ile-204 in SDL3, and internal ligand residue Thr-320 (Fig. 5*B*), which is invariantly Thr in β_2 integrin α subunits. Moreover, Pro-170 in SDL2 is in van der Waals contact with Tyr-115 in both closed and internally liganded β_2 integrin structures (Fig. 5*B*). Thus, movement of SDL1 enforces through Tyr-115 contact with Pro-170 a movement of similar or even greater magnitude in SDL2 (measured displacements at Cα atoms are 1.5 Å at Tyr-115 and 2.7 Å at Pro-170). Apparently, Pro-170 must move in the same direction as Tyr-115 rather than sideways, because the position of Pro-170 in SDL2 is constrained by the Cys-169 to Cys-176 disulfide internal to SDL2 and the adjacency of Pro-170 to Cys-169, which is in turn adjacent to another Pro, Pro168.

Sequence variation in SDL loop sequences correlates with β-subunit sequence variation overall, and four of eight human integrin β subunits have Tyr in the same position in SDL1 as β_2 Tyr-115 (17). The β-integrin most similar to β_2 is β_7. The β_2 Tyr-115–Pro-170 interaction is structurally conserved in β_7 as an interaction between Tyr-143 and Pro-198 (Fig. S2). However, the magnitude of movement of Tyr-143 and Pro-198 when the ligand is soaked in is much smaller, only 0.4 Å at the Tyr-143 C α atom. Tellingly, the $\alpha_4\beta_7$ headpiece was crystallized in the presence of a Fab that binds to an epitope in SDL2. Therefore, ligand-induced movement of SDL1 may have been limited by the constraints imposed by SDL2 contact and the Fab. In β_1, Tyr-133 in SDL2 contacts the disulfide bond of SDL2. When small ligands are soaked into $\alpha_5\beta_1$ crystals, the Tyr tends to move around the disulfide rather than displace it (Fig. S2). However, β_1 integrins bind a large variety of ligands and have both αI and αI-less α subunits; movements of SDL2 might be induced if external or internal ligands prevented sliding of Tyr-133 around the SDL2 disulfide.

An early study on RGD soaked into $\alpha_V\beta_3$ integrin crystals saw movement in both SDL1 and SDL2 (29), although the modeled SDL2 loop was inconsistent with its electron density (17) and the contact with Met-180 described below was not mentioned. Recently, higher resolution structures revealed the complete shape-shifting process for $\alpha_{IIb}\beta_3$ from closed to open with six intermediate, structurally defined steps (27). Examination of these structures for a contact similar to that found here in β_2 integrins shows that in $\alpha_{IIb}\beta_3$ opening, Tyr-122 in SDL1 maintains van der Waals contact with Met-180 in SDL2 (Fig. 5*C*) and causes SDL2 to move in concert with SDL1. Between the closed and open conformations, a 1.5 Å motion at the Tyr-122 backbone in SDL1 is associated with a 1.8 Å movement at the Met-180 backbone in SDL2. Although SDL2 does not contact peptide ligands soaked into $\alpha_V\beta_3$ or $\alpha_{IIb}\beta_3$ crystals (27, 29, 30), SDL2 might contact macromolecular ligands of these integrins. The similarity in concerted SDL1 and SDL2 movements in β_2 and β_3 integrins suggests that this mechanism for transmitting allostery between ligand-binding loops in integrins may hold for the half of integrin β subunits that have an equivalent Tyr residue in SDL1 and that include βI domains that bind both internal and external ligands.

Conclusion

High-resolution structures of the LFA-1 headpiece provide insights into αI domain flexibility and how αI domains interact with the α-subunit β-propeller and β-subunit βI domain in relay of allostery between αI and βI domains. Resolution of the binding pocket for the internal ligand in LFA-1 enables rational, structure-based design of α/βI allosteric antagonists with enhanced

α-subunit selectivity. The high-resolution view of $\alpha_L\beta_2$ with all three βI domain metal ions bound in comparison with internally liganded $\alpha_X\beta_2$ now reveals that in βI domain allostery, SDL2 moves in response to SDL1 and substantially tightens the binding pocket for the internal ligand. Movements of SDL2 linked to SDL1 also occur in $\alpha_{IIb}\beta_3$ and may provide a mechanism for tightening binding to external ligands as well as internal ligands.

Protein Expression, Purification, Crystallization, and Structure Determination

α_L subunit cDNA encoding mature residues Y1-N745 was cloned into the vector pcDNA3.1/Hygro. This coding sequence was followed by a 3C-protease site, the ACID coiled-coil, strep-tactin tag, and His_6 tag (27). β_2-subunit mature residues Q1-E460 followed by a 3C-protease site, the BASE coiled-coil, strepavidin binding peptide, and His_6 tag were inserted into vector ET1 (31). *N*-linked sites in α_L (six sites) and in β_2 (three sites) were individually tested for effects on transient expression of $\alpha_L\beta_2$ headpiece using capture ELISA. Individual elimination of two α_L sites (N645R and N701R) and one β_2 site (N232K) had no adverse effect. Combination of the three mutations resulted in transient expression at 55% of wild-type levels and was used in protein for crystallization.

Protein was expressed in HEK293S *N*-acetylglucosaminyl transferase I-negative ($GnTI^{-/-}$) cells (32). Culture supernatant supplemented with 20 mM Tris pH 8.2, 200 mM NaCl, and 0.25 mM $NiCl_2$ was centrifuged at 3,000 × *g*; concentrated about 10-fold using tangential flow with a 30,000 M_r cutoff; and loaded onto His tag affinity matrix by gravity (10 mL/1 L of culture supernatant). The column was pre-equilibrated in 20 mM Tris pH 8.0, 650 mM NaCl, 1 mM $CaCl_2$, 5 mM $MgCl_2$, and 13 mM imidazole (loading buffer). After washing the column with 10 column volumes of loading buffer, a Strep-tactin Sepharose (IBA, Olivette, MO) (2.5 mL/L supernatant) column was attached downstream, and the sample was eluted with 10 column volumes of loading buffer plus 250 mM imidazole. The Strep-tactin column was washed with 10 column volumes of 20 mM Hepes pH 7.0, 150 mM NaCl, 1 mM $CaCl_2$, and 5 mM $MgCl_2$ and eluted in the same buffer additionally containing 2.5 mM desthiobiotin. C-terminal tags were cleaved with GST-3C protease at 4 °C overnight (1:3 mass ratio GST-3C:headpiece). The digest was passed through sequential GST and His-tag resins. The flow-through was concentrated, further purified by S200 gel filtration, and stored at 4 °C for about 1.5 y (during which the thigh domain was proteolytically removed). After storage and a second S200 gel filtration, the $\alpha_L\beta_2$ headpiece was concentrated to ∼4 mg/mL in 10 mM Hepes pH 7, 150 mM NaCl, 1 mM $CaCl_2$, and 5 mM $MgCl_2$ and screened for crystallization using hanging drop vapor diffusion at 4 °C.

Three LFA-1 crystal structures were obtained in different buffers, all with polyethylene glycol (PEG) at 4 °C: 0.1 M Mg-formate dehydrate and 15% (wt/vol) PEG 3350 (pH of 6.8 as recorded in the Hampton production report); 0.1 M Tris, pH 8, 0.1 M NaCl, and 8% (wt/vol) PEG 20,000; and 0.1 M Mes, pH 6.5, and 15% (wt/vol) PEG 3350. Crystals were cryoprotected by transfer over 10 min to mother liquor containing 30% (vol/vol) glycerol in 5% glycerol increments and plunge-vitrified in liquid nitrogen. Diffraction data collected at APS beamline ID-23 were processed with XDS (33). The Tris structure was solved by molecular replacement (34) using the α_L αI domain (6) and head domains from $\alpha_X\beta_2$. An initial model was obtained by refining each domain as a rigid body followed by torsion angle simulated annealing. Many rounds were carried out of rebuilding with Coot (35), refinement with PHENIX (34), and validation with MolProbity (36).

ACKNOWLEDGMENTS. We thank Adem Koksal, Nathan Hudson, and Travis Moore for critical reading of this manuscript; Xianchi Dong for help with X-ray data acquisition; and the staff at Advanced Photon Source beamline 23-ID (GM/CA-CAT). This work was supported by NIH Grant NCI CA031798 and a GlaxoSmithKline fellowship.

1. Springer TA, Dustin ML (2012) Integrin inside-out signaling and the immunological synapse. *Curr Opin Cell Biol* 24(1):107–115.
2. Petruzzelli L, Luk J, Springer TA (1995) Adhesion structure subpanel 5, leukocyte integrins: CD11a, CD11b, CD11c, CD18. *Leucocyte Typing V: White Cell Differentiation Antigens*, eds Schlossman SF, et al. (Oxford Univ Press, New York), pp 1581–1585.
3. Springer TA (1990) Adhesion receptors of the immune system. *Nature* 346(6283):425–434.
4. Anderson DC, Springer TA (1987) Leukocyte adhesion deficiency: An inherited defect in the Mac-1, LFA-1, and p150,95 glycoproteins. *Annu Rev Med* 38:175–194.
5. Gottlieb AB, et al. (2002) Psoriasis as a model for T-cell-mediated disease: Immunobiologic and clinical effects of treatment with multiple doses of efalizumab, an anti-CD11a antibody. *Arch Dermatol* 138(5):591–600.
6. Qu A, Leahy DJ (1995) Crystal structure of the I-domain from the CD11a/CD18 (LFA-1, alpha L beta 2) integrin. *Proc Natl Acad Sci USA* 92(22):10277–10281.
7. Qu A, Leahy DJ (1996) The role of the divalent cation in the structure of the I domain from the CD11a/CD18 integrin. *Structure* 4(8):931–942.
8. Shimaoka M, et al. (2003) Structures of the α L I domain and its complex with ICAM-1 reveal a shape-shifting pathway for integrin regulation. *Cell* 112(1):99–111.
9. Song G, et al. (2005) An atomic resolution view of ICAM recognition in a complex between the binding domains of ICAM-3 and integrin alphaLbeta2. *Proc Natl Acad Sci USA* 102(9):3366–3371.
10. Zhang H, et al. (2008) An unusual allosteric mobility of the C-terminal helix of a high-affinity alphaL integrin I domain variant bound to ICAM-5. *Mol Cell* 31(3):432–437.
11. Legge GB, et al. (2000) NMR solution structure of the inserted domain of human leukocyte function associated antigen-1. *J Mol Biol* 295(5):1251–1264.
12. Leung HT, et al. (2014) NMR characterization of the conformational fluctuations of the human lymphocyte function-associated antigen-1 I-domain. *Protein Sci* 23(11):1596–1606.
13. Xie C, et al. (2010) Structure of an integrin with an alphaI domain, complement receptor type 4. *EMBO J* 29(3):666–679.
14. Shi M, et al. (2005) The crystal structure of the plexin-semaphorin-integrin domain/hybrid domain/I-EGF1 segment from the human integrin β2 subunit at 1.8-A resolution. *J Biol Chem* 280(34):30586–30593.
15. Shi M, et al. (2007) A structural hypothesis for the transition between bent and extended conformations of the leukocyte β2 integrins. *J Biol Chem* 282(41):30198–30206.
16. Sen M, Yuki K, Springer TA (2013) An internal ligand-bound, metastable state of a leukocyte integrin, $\alpha_X\beta_2$. *J Cell Biol* 203(4):629–642.
17. Dong X, et al. (2012) $\alpha_V\beta_3$ integrin crystal structures and their functional implications. *Biochemistry* 51(44):8814–8828.
18. DiMaio F, et al. (2013) Improved low-resolution crystallographic refinement with Phenix and Rosetta. *Nat Methods* 10(11):1102–1104.
19. Yu Y, et al. (2012) Structural specializations of $\alpha_4\beta_7$, an integrin that mediates rolling adhesion. *J Cell Biol* 196(1):131–146.
20. Zhu J, et al. (2008) Structure of a complete integrin ectodomain in a physiologic resting state and activation and deactivation by applied forces. *Mol Cell* 32(6):849–861.
21. Nagae M, et al. (2012) Crystal structure of $\alpha_5\beta_1$ integrin ectodomain: Atomic details of the fibronectin receptor. *J Cell Biol* 197(1):131–140.
22. Dong X, Hudson NE, Lu C, Springer TA (2014) Structural determinants of integrin β-subunit specificity for latent TGF-β. *Nat Struct Mol Biol* 21(12):1091–1096.
23. Xia W, Springer TA (2014) Metal ion and ligand binding of integrin $\alpha_5\beta_1$. *Proc Natl Acad Sci USA* 111(50):17863–17868.
24. Kishimoto TK, O'Connor K, Lee A, Roberts TM, Springer TA (1987) Cloning of the β subunit of the leukocyte adhesion proteins: Homology to an extracellular matrix receptor defines a novel supergene family. *Cell* 48(4):681–690.
25. Weitz-Schmidt G, Schürpf T, Springer TA (2011) The C-terminal αI domain linker as a critical structural element in the conformational activation of αI integrins. *J Biol Chem* 286(49):42115–42122.
26. Shimaoka M, Springer TA (2003) Therapeutic antagonists and conformational regulation of integrin function. *Nat Rev Drug Discov* 2(9):703–716.
27. Zhu J, Zhu J, Springer TA (2013) Complete integrin headpiece opening in eight steps. *J Cell Biol* 201(7):1053–1068.
28. Kamata T, et al. (2002) The role of the CPNKEKEC sequence in the β_2 subunit I domain in regulation of integrin $\alpha_L\beta_2$ (LFA-1). *J Immunol* 168(5):2296–2301.
29. Xiong JP, et al. (2002) Crystal structure of the extracellular segment of integrin $\alpha_V\beta_3$ in complex with an Arg-Gly-Asp ligand. *Science* 296(5565):151–155.
30. Springer TA, Zhu J, Xiao T (2008) Structural basis for distinctive recognition of fibrinogen γC peptide by the platelet integrin $\alpha_{IIb}\beta_3$. *J Cell Biol* 182(4):791–800.
31. Mi LZ, et al. (2008) Functional and structural stability of the epidermal growth factor receptor in detergent micelles and phospholipid nanodiscs. *Biochemistry* 47(39):10314–10323.
32. Reeves PJ, Callewaert N, Contreras R, Khorana HG (2002) Structure and function in rhodopsin: High-level expression of rhodopsin with restricted and homogeneous N-glycosylation by a tetracycline-inducible N-acetylglucosaminyltransferase I-negative HEK293S stable mammalian cell line. *Proc Natl Acad Sci USA* 99(21):13419–13424.
33. Kabsch W (2001) F, crystallography of biological macromolecules. *International Tables for Crystallography*, eds Rossmann MG, Arnold E (Kluwer Academic Publishers, Dordrecht, The Netherlands), pp 730–734.
34. Adams PD, et al. (2010) PHENIX: A comprehensive Python-based system for macromolecular structure solution. *Acta Crystallogr D Biol Crystallogr* 66(Pt 2):213–221.
35. Emsley P, Cowtan K (2004) Coot: Model-building tools for molecular graphics. *Acta Crystallogr D Biol Crystallogr* 60(Pt 12 Pt 1):2126–2132.
36. Davis IW, et al. (2007) MolProbity: All-atom contacts and structure validation for proteins and nucleic acids. *Nucleic Acids Res* 35(Web Server issue):W375–W383.
37. Karplus PA, Diederichs K (2012) Linking crystallographic model and data quality. *Science* 336(6084):1030–1033.

Supporting Information

Springer and Sen 10.1073/pnas.1601379113

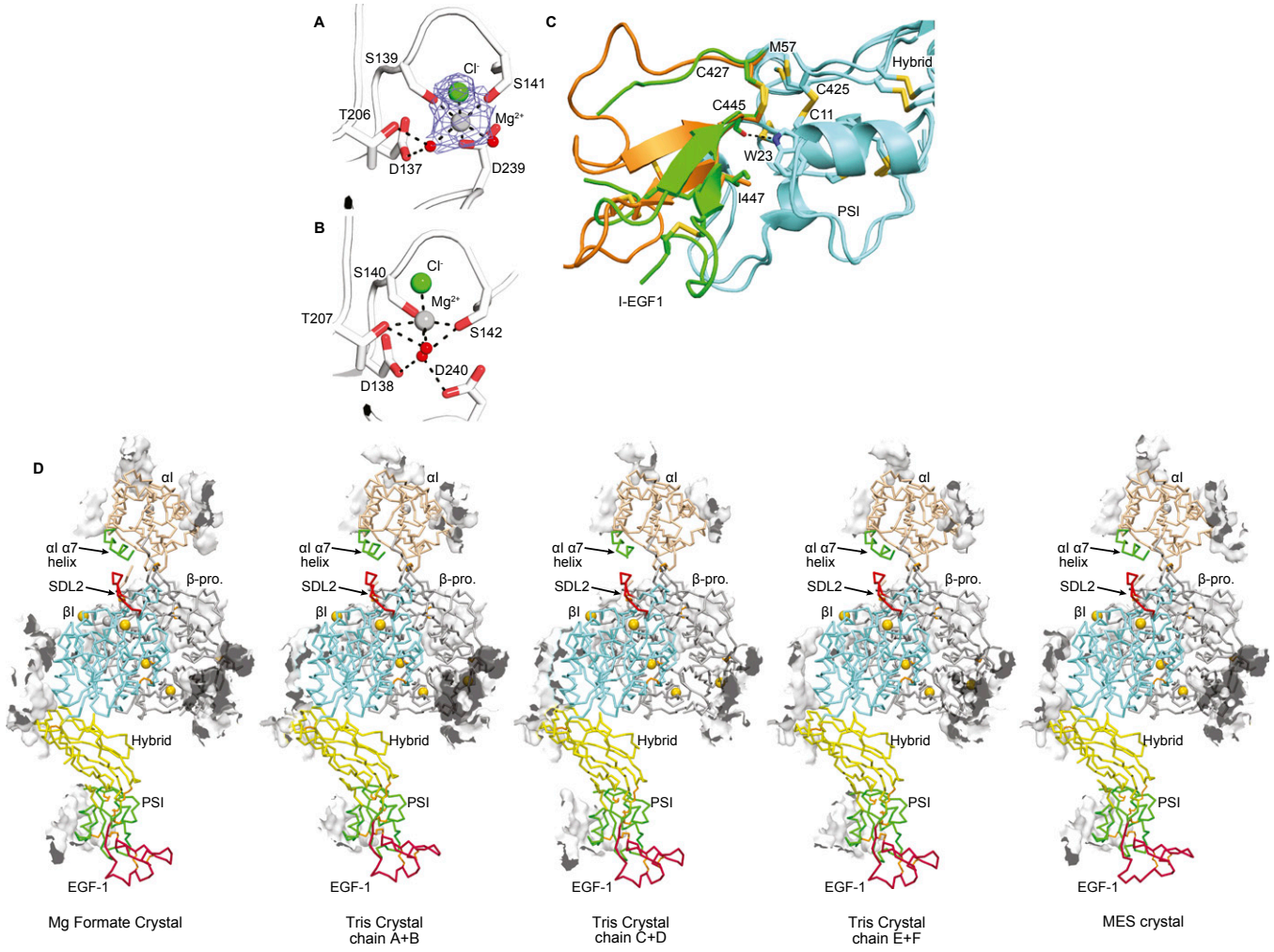

Fig. S1. Structural details. (*A* and *B*) The closed αI MIDAS of the $\alpha_L\beta_2$ headpiece (PDB ID code 5E6U) (*A*) and the open αI MIDAS of internally liganded, cocked $\alpha_X\beta_2$ (PDB ID code 4NEH) (*B*) in identical orientations after superimposition on the αI domain. Mg^{2+}, water, and Cl^- are shown as silver, red, and green spheres, respectively. Mesh in *A* shows simulated annealing omit map density for Mg^{2+} and Cl^- ions at 1σ. (*C*) Flexion in the middle of the I-EGF1 domain. I-EGF1 domains from β_2-leg fragments are green (PDB ID code 5E6W) and orange (PDB ID code 5E6V). PSI and hybrid domains are cyan. (*D*) Contacts in the crystal lattice within 4 Å of the LFA-1 headpiece (PDB ID code 5E6U) are shown as white surfaces. The lattice interaction of the αL I-domain is 584 Å2.

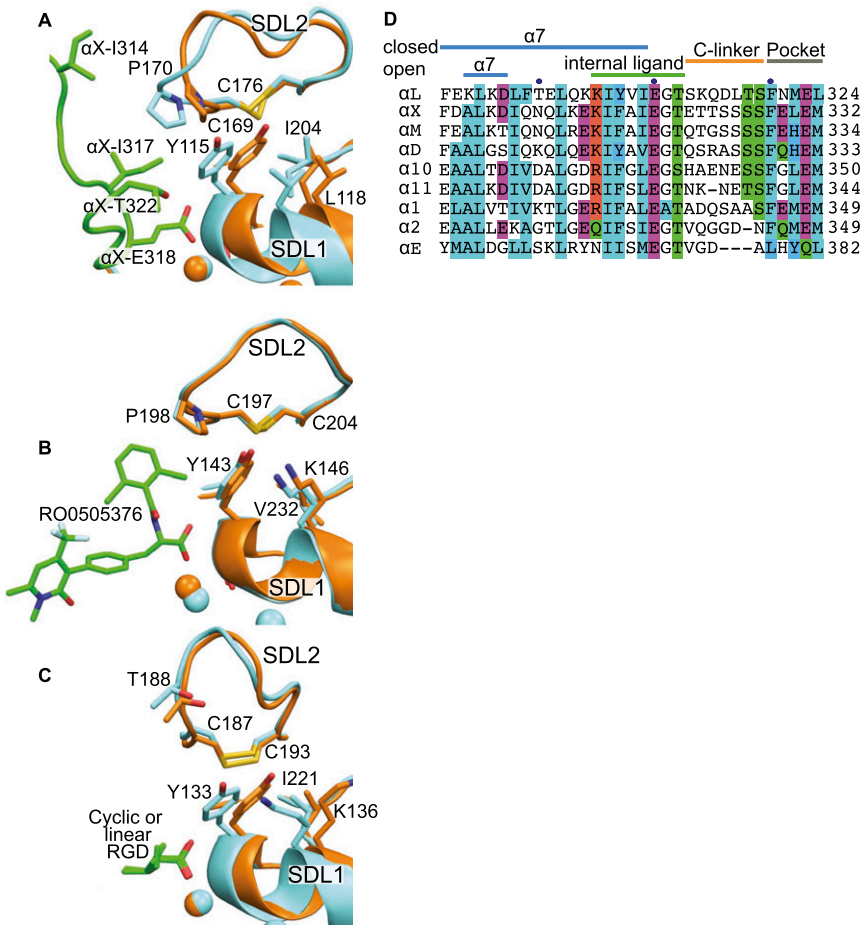

Fig. S2. Interactions between SDL1 and SDL2 in intermediate crystal structures and αI integrin sequences around the internal ligand and its binding pocket. (*A*–*C*) Superimpositions based on the integrin head in identical orientations showing SDL1 and SDL2, with closed integrins in orange, intermediate integrins in cyan, and ligands in green. Ribbon cartoons show ligands and key side chains in stick; βI MIDAS metal ions are spheres in the same color as integrins. (*A*) Closed $\alpha_L\beta_2$ (PDB ID code 5E6U) and internally liganded, cocked $\alpha_X\beta_2$ (PDB ID code 4NEH) (18). (*B*) Closed $\alpha_4\beta_7$ (PDB ID code 3V4P) and intermediate RO0505376-bound $\alpha_4\beta_7$ (PDB ID code 3V4V) (21). (*C*) Closed, GRGDSP peptide-bound $\alpha_5\beta_1$ (PDB ID code 4WK0) and intermediate, cyclic-RGD peptide-bound $\alpha_5\beta_1$ (PDB ID code 4WK4) (25). (*D*) Sequences of all human αI integrins around the pocket, internal ligand, and C-linker.

Table S1. Data collection and refinement statistics*

	Mg formate	Tris	Mes
Data collection			
Space group	$P6_1$	$P2_1$	$P6_1$
Cell dimensions			
a, *b*, *c*, Å	154.9, 154.9, 118.4	151.9, 118.6, 151.9	153.9, 153.9, 116.5
α, β, γ, °	90, 90, 120	90, 118.6, 90	90, 90, 120
Resolution, Å	50–2.5	50–2.15	50–2.9
$CC_{1/2}$, %[†]	98.8 (11.4)	98 (10.1)	99.6 (13)
R_{merge}[‡]	19 (211)	17.6 (199)	9.3 (168)
I/σ, *I*	6.2 (0.45)	5.2 (0.47)	9.47 (0.47)
Completeness, %	99.5 (96.3)	70.5 (34.7)	97.8 (85.3)
Redundancy, %	5.2 (2.8)	2.8 (1.9)	3.11 (1.88)
Refinement			
Resolution, Å	50–2.5	50–2.15	50–2.9
No. reflections, total/unique	282,303 (54,239)	510,372 (180,557)	105,809 (33,986)
% R_{work}[§]/R_{free}[¶]	17.9/22.5	19.4/23.4	19.3/22.9
No. atoms			
Protein	8,081	24,146	7,997
Ion	7	18	5
Water	654	2,052	206
B factors			
Protein	53	38	85
Ion	44	48	92
Water	51	39	71
Mol/asym unit	1	3	1
Ramachandran, %[#]	96.1, 3.7, 0.2	95.7, 4.0, 0.3	94.7, 4.8, 0.5
MolProbity score	1.67 (99%)	1.74 (94%)	1.78 (100%)
MolProbity ClashScore	5.6 (99%)	5.24 (97%)	4.85 (100%)
rmsd			
Bond lengths, Å	0.007	0.004	0.012
Bond angles, °	0.762	0.800	0.788
PDB ID code	5E6U	5E6S	5E6R

*Numbers in parentheses correspond to the outermost resolution shell.

[†]$CC_{1/2}$, Pearson's correlation coefficient between average intensities of random half-datasets for each unique reflection (37).

[‡]$R_{merge} = \Sigma hkl \Sigma i |Ii(hkl) - \langle I(hkl)\rangle| / \Sigma hkl \Sigma i Ii(hkl)$, where $Ii(hkl)$ and $\langle I(hkl)\rangle$ are the *i*th and mean measurement of the intensity of reflection *hkl*.

[§]$R_{work} = \Sigma hkl ||F_{obs}(hkl)| - |F_{calc}(hkl)|| / \Sigma hkl |F_{obs}(hkl)|$, where $F_{obs}(hkl)$ and $F_{calc}(hkl)$ are the observed and calculated structure factors, respectively. No I/σ cutoff was applied.

[¶]R_{free} is the *R* value obtained for a test set of reflections consisting of a randomly selected ~5% subset of the dataset excluded from refinement.

[#]Residues in favored, accepted, and outlier regions of the Ramachandran plot as reported by MolProbity (36).

Table S2. Rerefinement statistics*

	$\alpha_X\beta_2$		β_2 hybrid+PSI+EGF1		β_2 hybrid+PSI+EGF1–2		β_2 hybrid+PSI+EGF1–3	
Data collection								
Space group	$P2_12_12_1$	$P2_12_12_1$						
Cell dimensions								
a, *b*, *c*, Å	132.1, 163.6, 536.9	132.0, 163.5, 536.4						
α, β, γ, °	90, 90, 90	90, 90, 90						
Resolution, Å	48.6–3.56	49.5–3.15						
$CC_{1/2}$[†]	Not reported	99.8 (12)						
R_{merge}[‡]	16.1 (137.1)	20.5(876)						
$I/\sigma I$	12.0 (1.9)	9.46(0.2)						
Completeness, %	99.9 (100.0)	98.6(84.8)						
Redundancy, %	7.6 (N/A)	7.2(4.9)						
No. reflections, total/unique	1,108,987 (147,271)	1,431,576 (198,644)						
Refinement statistics								
Resolution range, Å	48.6–3.56	49.5–3.3	30–1.8	30–1.8	27.8–1.75	27.8–1.75	25–2.2	25–2.2
R_{work}, %[§]	29.7	25.8	23.4	17.7	20.4	19.7	26.1	22.2
R_{free}, %[¶]	33.5	30.8	25.3	22.9	25.3	24.5	30.8	27.6
Model statistics								
rmsd								
Bond lengths, Å	0.003	0.007	Not reported	0.009	Not reported	0.003	Not reported	0.004
Bond angles, °	0.648	1.204	Not reported	1.123	Not reported	0.725	Not reported	0.923
Ramachandran plot, favored/allowed/outlier[#]	76.3/21.4/2.3	89.8/8.3/1.9	9.6/2/1.4	98/2/0	97.1/1.8/1.1	97.8/2.2/0	95.3/4.7/0	96/4/0
MolProbity percentile, Clashscore/geometry[§]	86/95	97/100	45/32	99/99	87/52	95/98	98/62	99/96
Number of residues	6,432	6,427	214	224	280	280	310	310
Number of metals	17	17	0	0	0	0	0	0
Number of carbohydrates	42	112	2	5	3	3	1	2
Number of *cis*-peptides	22	22	1	1	6	1	2	1
Number of waters	3	67	219	235	268	260	199	185
PDB ID code	3K6S	5ES4	1YUK	5E6V	2P26	5E6X	2P28	5E6W

*Numbers in parentheses correspond to the outermost resolution shell.

[†]$CC_{1/2}$, Pearson's correlation coefficient between average intensities of random half-datasets for each unique reflection (37).

[‡]$R_{merge} = \Sigma hkl\Sigma i|Ii(hkl) - \langle I(hkl)\rangle|/\Sigma hkl\Sigma iIi(hkl)$, where $Ii(hkl)$ and $\langle I(hkl)\rangle$ are the *i*th and mean measurement of the intensity of reflection *hkl*.

[§]$R_{work} = \Sigma hkl||F_{obs}(hkl)| - |F_{calc}(hkl)||/\Sigma hkl|F_{obs}(hkl)|$, where $F_{obs}(hkl)$ and $F_{calc}(hkl)$ are the observed and calculated structure factors, respectively. No I/σ cutoff was applied.

[¶]R_{free} is the *R* value obtained for a test set of reflections consisting of a randomly selected ~5% subset of the dataset excluded from refinement.

[#]Residues in favored, accepted, and outlier regions of the Ramachandran plot as reported by MolProbity (36).